Statistically-motivated, Iterative Image Reconstruction Algorithm for Proton Computer Tomography Applications

Ákos Sudár

Medical Physicist, Faculty of Nuclear Techniques,

Budapest University of Technology and Economics,

Research Engineer, Wigner Research Centre for Physics

Supervisor:

Mónika Varga-Kőfaragó, Ph.D.

Researcher, Hadron Physics Research Group, Department for High Energy Particle Physics,

Institute for Particle and Nuclear Physics, Wigner Research Centre for Physics

Consultants:

Dr. Dávid Légrády

Associate professor, Faculty of Nuclear Techniques,

Budapest University of Technology and Economics,

Gergely Gábor Barnaföldi, Ph.D.

Group leader, Heavy-ion Physics Research Group, Department for Theoretical Physics,

Institute for Particle and Nuclear Physics, Wigner Research Centre for Physics

Budapest, 2021

Abstract

Modern proton Computed Tomography (pCT) images are usually reconstructed by the algebraic reconstruction techniques (ART). The Kaczmarz-method and its variations are among the most used methods, which are iterative solution techniques for linear problems with sparse matrices. It is an interesting question whether statistically-motivated iterations, which have been successfully used for emission tomography, can be applied to reconstruct for a novel technology of pCT images as well.

In my research, I developed a method for pCT image reconstructions, based on the Richardson–Lucy deconvolution – as a statistically-motivated fixed-point iteration. I implemented this algorithm to a parallel GPU code, with spline-based trajectory calculation and on-the-fly system matrix generation. My results presented that the method works well, and it can be successfully applied in pCT applications, such as in the detector R&D of the Bergen pCT Collaboration.

Contents

1 Introduction

Cancer has the highest mortality, especially in the developed countries, so the need to have effective treatments and therapies against it is increasingly important. One of the widely-applied treatment for cancer is the radiotherapy. Recently the interest is growing for a novel technology, hadron therapy, mainly using proton beams for the therapy. Applying high-energy protons it is possible to focus the delivered dose more on the tumor, better than the standard radiotherapy methods using MeV-energy photons.

One of the main direction in the development of proton therapy is to increase the accuracy of treatment planning, which is important to reduce dose and focus the damage on the target tissues. The limitation of the treatment planning is the accuracy of the relative stopping power (RSP) distribution map of the patient. Today these maps are generally converted from X-ray CT images, with the use of conversion tables between Hounsfield unit (HU) and RSP. This conversion is not trivial in the typical range of Hounsfield units of the human body, therefore conversion can significantly increase the error of the final RSP map, which can cause up to 1.7 % statistical error. This error can be reduced to 0.5 % with the use of pCT imaging [1].

The proton CT scanner designs usually use movable treatment beam as proton source and a proper detector system to measure the protons. A typical detector has two functionality:

1. The first is to measure the remaining energy of the protons behind the patient. If it is built of energy sensitive detectors it is called proton calorimeter (as it measures the energy of protons), if it is built of alternating detector and energy absorber layers it is usually called range counter (as it measures the remaining water equivalent range of the protons).

2. The second functionality is the measurement of the incoming and outcoming directions of protons, with pairs of tracking detectors, which infromation is necessary for the re-construction of the RSP map. The tracker detector pair in front of the patient is called forward tracking detector, the ones behind the patient called backward tracking detector. Sometimes the forward tracking detector is left out. In one hand this concept is advan-

3

tages because makes it possible to one event to contain certain number of protons, and this design is also more advantages from the point of view of the application in a treatment facility as it not interact with the beam during the treatment. On the other hand the this concept is less accurate in terms of investigating the trajectory of protons in the patient, than the concept, which contains both forward and backward tracker. Because its advantages the concept without forward tracker will be investigated in this work.

My TDK research was dedicated to this investigation, especially contributing to the detector development of the Bergen proton CT group in which I am member.

2 The Proton CT

The idea of proton CT was born the same time with the idea of X-ray CT, as both of them were suggested by A.M. Cormack in 1963. One of the original motivation behind both CT imaging was the dose planning for radiation therapy. Cormack realised the importance of pCT images for proton treatment planning to focus the Bragg peak into the tumor [2]. The first reasonable CT image was reconstructed by Cormack in 1964, it was about a phantom made of aluminum and Lucite cylinders and rings [3]. Indeed the experimental design has been already presented, only today state-of-the-art detector, accelerator and IT technologies led us to apply this in general in every-day treatment.

2.1 Motivation to pCT

The number of proton treatment centers is rapidly increasing [4] thanks to the fact that hadron beams can have more focused dose distribution compared with MeV-photon therapy [5, 6]. The motivation to make proton treatment more accurate is evolving in parallel with the number of treatment facilities, as more and more hospital could gain an advantage of a novel device, technology or a treatment method. There are lot of possible directions for improvement in this research field, including but not limited to patient positioning and movement monitoring, use of Monte Carlo in dose planning [7], pCT imaging for the more accurate dose planning [2, 4, 8] and *in vivo* dosimetry for monitoring the dose distribution during and after the treatment [7, 9, 10].

2.2 The Bergen pCT Collaboration

The Bergen pCT Collaboration, is an international collaboration with a centrum in the University of Bergen, Bergen, Norway. It was established to develop a pCT system, based on the detector technologies used at high-energy particle detector at CERN or in other international collaborations. This applied study aims to reach the clinical testing phase, which has never been reached so far. Since the early beginning the Wigner Research Centre for Physics has

been joint to this effort, and I – as a member for he group – could personally participate from the development of the Bergen pCT detector prototype.
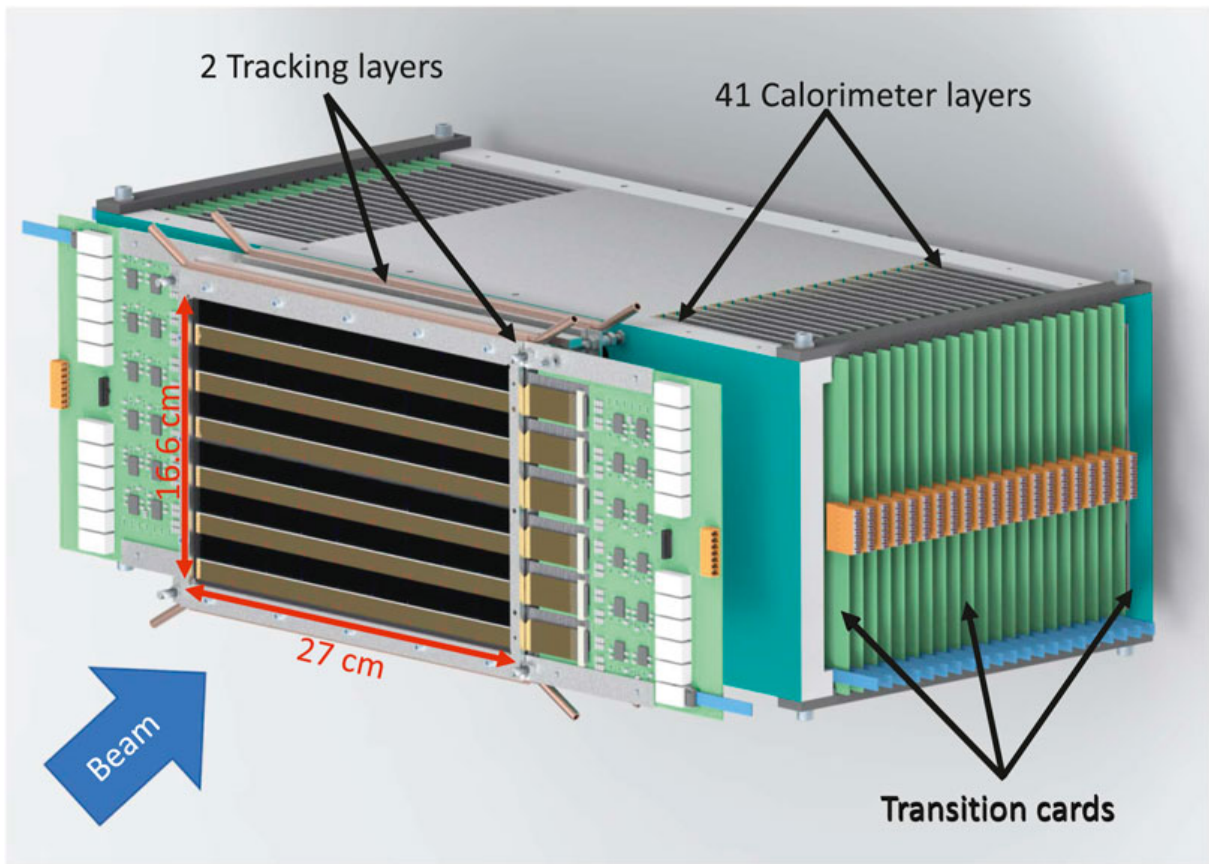
Figure 1: The design of the Bergen pCT detector system. The beam comes from the left hand side, the tracker lsyer pair is visible in the foreground, the 41 layers of the Digital Tracking Calorimeter (DTC) is in the background, and the transition cards of the readout electronics is set in the sides [11].

The main concept of the pCT detector system is to use the technology of the silicon pixel tracker detectors for the measurement of the direction and the remaining energy of the protons. The challenge of this is that the energy range here is few magnitude lower, than the original design of this detector in high-energy physics. Here, the direction of the protons measured only after the patient, which makes it possible to measure 100 protons in each frame in the area of a pencil beam with 7 mm full width at half maximum (FWHM). The lack of information resulted

by the shortage on the forward tracker is partially compensated with the very accurate rear tracker [12]. The accuracy of the rear tracker pair comes from the high spatial resolution of the tracker detector (~ 5 μm) and the low material budget of the tracker layers: the thickness of the detector and the support structure are 50 μm and 200 μm, respectively. The energy measurement is based on a range counter design, so alternating tracker detector and absorber layers are implemented. The number of firing pixels in the tracker detector, when a proton goes through it, contains some information about the deposited energy in the tracker detector. The energy measurement based on the fit of a Bragg curve into these energy deposits, makes possible a more accurate energy measurement, than the number of traversed layers would allow.

The pCT detector system is based on the ALPIDE chip, which is a monolithic active pixel sensor (MAPS) type silicon pixel detector [13]. This contains the sensitive sensors together with the readout electronics on the same silicon layer. ALPIDE was developed for the Inner Tracking System (ITS) of 'A Large Ion Collider Experiment' (ALICE), which is one of the four giant experimental facilities of the Large Hadron Collider (LHC) at the European Organization for Nuclear Research (CERN), Geneva, Switzerland.

The Bergen pCT Collaboration had a previous range counter design, which was the proof-of-concept Digital Tracking Calorimeter (DTC) in pCT application. The measurements confirmed the concept, as it reached 4% accuracy in terms of the measurement of the remaining water equivalent thickness (WET) of the protons and showed 10^6 proton per second performance based on MC simulations, which is in the higher end of the sensitivity and time resolution of the pCT prototypes [14]. The group continued the work with the design study of a next, more optimized pCT detector [8]. The new concept contains two tracker layers, and 41 alternating aluminium absorber and tracker detector layer, which is an optimum between accuracy and cost. The detector is designed to measure 10^7 individual proton tracks in each second with the use of a 7 mm FWHM pencil beam.

The research and development work is still in progress, following the plansof the Bergen pCT Collaboration. Today the design and the detailed investigation of the detector concept is ongoing. The new prototype is in the construction phase now [11]. In parallel the track

reconstruction and data analysis software development has been started, in which I am also participating.

2.3 My contribution to the Bergen pCT project

I was actively involved in the measurement of the relation between the particle energy (which determines the expected energy deposition) and the number of firing pixels. We took the data in two test beam measurement with proton, helium, and carbon ion beams in the Heidelberg Ion-beam Therapy Center (HIT). In Figure 2 the points represent the mean value of the Normal distribution fitted into the measured cluster size distribution on the silicon pixel detector. Meanwhile the bars are for the standard deviation of the fitted distribution, so these stand for the representation of the width of the distribution and not for the error of the mean value. We found clear relation by the following equation [15, 11]:

$$N = 2.40 \cdot \Delta E^{0.338} \ , \tag{1}$$

where N is the number of firing pixels (called cluster size) and ΔE is the expected deposited energy. The constant factor 0.338 was determined by fitting the measured data, as presented in Figure 2. My main contribution was the data analysis of the measurement, which resulted in the data points and appeared in publications of the collaboration [15, 11] and in my previous OTDK thesis [16].
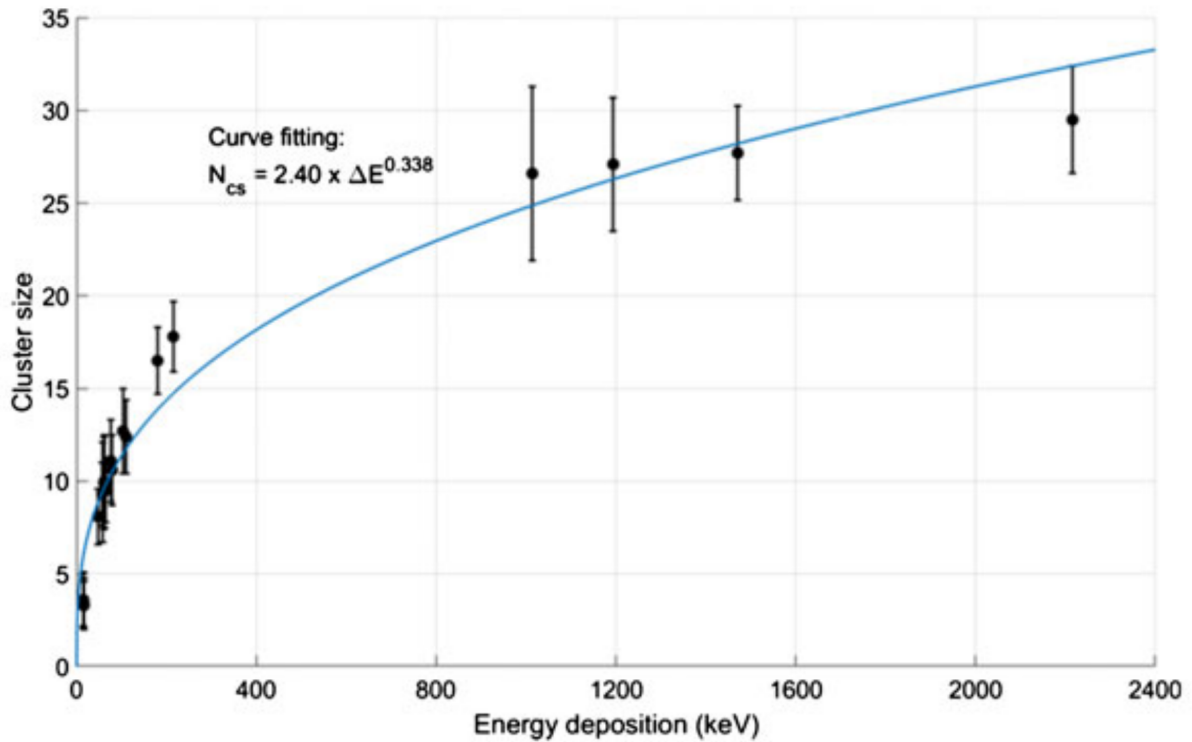
Figure 2: The measured cluster size in function of expected deposited energy [11].

My further contribution is the study of two cooling system concepts for the range detector. I used analytical calculations and finite element simulations for modeling the temperature distribution inside the range detector. My results appears in one of the status report publications of the collaboration [11], in one of my previous TDK thesis [17], and in my BSc thesis [18].

My current contribution is the investigation of the application of statistically motivated iterative methods for image reconstruction. This has been first discussed in this present TDK work. So far there is no such analysis known publicly available in the international literature.

3   Image Reconstruction Methods

During proton CT imaging we collect information about the relative stopping power (RSP) of the phantom or patient through some trajectories. The role of image reconstruction is to determine the original the RSP distribution of the imaged object. There are two main direction of reconstruction CT images, the first based on integral transformations. The first representative of this kind was the Radon and the Inverse Radon transformation published by Johann K. A. Radon in 1917 [19]. The CT reconstruction techniques introduced by A. M. Cormack [2, 3] are belongs to this group. The second main direction is to model the problem as a linear equation system, and solve it with the use of iterative algorithms. This direction was introduced and called Algebraic Reconstruction Technique (ART) in image reconstruction by Gordon, Bender and Herman in 1970. The Richardson-–Lucy deconvolution [20, 21] is also an iterative reconstruction technique can be applied for reconstruction of CT image. This algorithm is mainly used in emission tomography, and first applied for pCT image reconstruction in the current work.

3.1   Introduction to iterative image reconstruction techniques

If we reconstruct the image in discrete voxels, than the image reconstruction can be written in the following algebraic form:

$$\mathbf{y} = \mathbf{A} \cdot \mathbf{x}, \tag{2}$$

where $\mathbf{y}$ is an m-dimensional vector (typically $10^8 - 10^9$), which contains the water equivalent path length (WEPL) reduction of the protons in the reconstruction area, $\mathbf{x}$ is an n-dimensional vector (typically $10^5 - 10^7$) containing the RSP of the voxels, and finally $\mathbf{A}$ is an n × m matrix (also called system matrix, typically $10^{13} - 10^{16}$) which contains the interaction coefficient between protons and voxels. The information in $\mathbf{A}$ matrix can be describes as the length of the proton path in the voxel. In practice for the real cases n is larger than m. The goal of the image reconstruction is to investigate the values of $\mathbf{x}$ with the knowledge of $\mathbf{y}$ and $\mathbf{A}$. Typically, to obtain high-enough resolution, the size of the matrix is too large to use standard

matrix inversion like e.g. the pseudo inverse method. On the other hand, the matrix is sparse, which property can be used to find an effective way for the solution of the linear problem. In the literature orthogonal projection based iterative algorithms are widely used in Refs. [4, 22, 23, 24, 25]. A short review is given in the following subsections.

3.2 Diagonally Relaxed Orthogonal Projection (DROP) Method

In the literature usually different variations of the DROP method appears for pCT image reconstruction. The predecessor of these methods in linear algebra is the Kaczmarz [26] iteration, which was rediscovered in the field of image reconstruction by Richard Gordon, Robert Bender, and Gábor Herman in the name of Algebric Reconstruction Tecnique (ART) [22]:

$$\rho_{i,j}^{q+1} = \max \left[\rho_{i,j}^{q} + \left(R_{k,\theta} - R_{k,\theta}^{q} \right) / N_{k,\theta}, \ 0 \right], \tag{3}$$

for (i,j) in ray (k,θ), where q stands for the number of iteration, (i,j) is the index of the voxels, (k,θ) is the index of the kth ray in projection θ, ρ is the density matrix of the voxels, R is the matrix of the integrated density along the rays,

$$R_{k,\theta}^{q} = \sum_{(i,j) \ \text{in ray} \ (k,\theta)} \rho_{i,j}^{q} \tag{4}$$

is the estimate of the integrated density along ray (k,θ) in iteration q and finally $N_{k,\theta}$ is the number of voxels crossed by ray (k,θ).

A more recent, DROP iteration scheme is also known following Ref. [24]:

$$x^{k+1} = x^{k} + \frac{\lambda_k}{m} \sum_{i=1}^{m} \frac{b_i - \langle A_i, x^k \rangle}{\|A_i\|_2^2} a_i \ , \tag{5}$$

where k is the number of iteration, x is the vector of the voxel values, λ^k is the relaxation parameters (constant or diagonal matrix), m is the number of trajectories, i is the index of trajectories, b is the vector of integrated values along trajectories, A is the interaction coefficient between the trajectories and the voxels and $\|...\|_2$ is the Euclidean norm. The DROP iteration defined in equation (5) has more advantage over the original ART iteration defined in equation (3), since it can take into account different interaction coefficients between the voxels and

trajectories. One can reach better convergence with the use of relaxation parameters, which can be changed during the iteration and one can easily parallelise the evaluation of equation (5) thanks to the independent elements of the sum.

3.3 Total Variation Superiorization of DROP Method

This subsection is a brief summary of the work of Penfold et $al.$ [23]. The main idea of this method is to try to find a solution, which minimize better by applying a merit function.

$$x^{k+1} = \mathbf{P}_{t(k)}(x^k) = x^k + \lambda_k U_{t(k)} \sum_{i \in I_{t(k)}} \frac{b_i - \langle a_i, x^k \rangle}{\|a_i\|_2^2} a_i \tag{6}$$

where $U_{t(k)} = \text{diag}\left(\left(1, 1/h_j^t\right)\right)$, where h_j^t is the number of proton trajectories which intersect the jth voxel in the tth block.

The merit function can be given as

$$\phi(p^k) = \sum_{g=1}^{J-1} \sum_{l=1}^{J-1} \sqrt{\left(p_{g+1,l}^k - p_{g,l}^k\right)^2 + \left(p_{g,l+1}^k - p_{g,l}^k\right)^2} \tag{7}$$

Schematic steps of the total variation superiorization of DROP Method following [23]:

set k = 0 and set $x^k = x_{FBP}$ the initial FBP reconstruction, and $\beta_k = 1$

repeat for 10 cycles

set s to a subgradient of ϕ at x^k

if $\|s\| > 0$ set $v^k = \frac{-s}{\|s\|}$ else set $v_k = s$ set continue = true while continue set $y^k = x^k + \beta_k v^k$

calculate the merit function (total variation), and if $\phi(y^k) \leq \phi(x^k)$

apply sequentially M times the projection operator $P_{t(k)}$ to y^k

calculate the feasibility proximity with using values from all earlier M blocks, and

$Pr(\mathbf{P}_M y) < Pr(x^k)$ set $x^{k+1} = \mathbf{P}_M y$

set continue = false, else set $\beta_k = \beta_k/2$

else set $\beta_k = \beta_k/2$

3.4 The Richardson — Lucy Algorithm

There is a different solution strategy, which model the problem from probability theory direction, and called Maximum Likelihood – Expectation Maximalization (ML-EM) method. This theory was successful in case of emission tomography, and it results also in an iteration cycle for the image reconstruction, called Richardson – Lucy deconvolution [20, 21]. This iteration cycle can be deduced from ML-EM theory in case of emission tomography, but known as a fixed-point iteration as well. The iterative solution is based on the formula,

$$x_i^{k+1} = x_i^k \frac{1}{\sum\limits_j A_{i,j}} \sum_j \frac{y_j}{\sum\limits_l A_{l,j} x_l^k} A_{i,j} \; , \tag{8}$$

for every i in N, where N is the length of vector x, which contains the RSP of the voxels, k is the number of iteration, A matrix contains the interaction coefficients between the proton trajectories and the voxels, j is the index of the trajectories in M, which is the number of the trajectories, y contains the integrated RSP along the trajectories, which is equivalent with the WEPL reduction of the protons travelling along the trajectories. The $y_j \; / \; \sum\limits_l A_{l,j} x_l^k$ term is usually called Hadamard ratio, represents the ratio of the integrated RSP along the proton path and its estimate, based on the voxel values calculated in the previous iteration.

The ML-EM problem for proton CT imaging is not solved by now. As long as that iteration is not introduced the Richardson – Lucy deconvolution can be used as a fixed-point iteration for pCT image reconstruction as a linear problem. Therefore, my work is the first step to use statistical based iterations in pCT image reconstruction, but it can motivate further developments in this research direction.

4 Model of the Image Reconstruction

In this section I will introduce the main details of the pCT image reconstruction model developed in this work. The first part of this section will summarize the details of the model of the physics implementation in my work. I applied Richardson – Lucy algorithm for restore the images. The elements of the system matrix, which represents the physical interaction between the protons and the voxels, was set based on this model. The second part of this section details the computational model of the problem, which contains the on-the-fly calculation of the system matrix elements and the Richardson – Lucy iteration itself. In this model I implemented on-the-fly matrix calculation, because even the zero suppressed system matrix could reach the size of 10^{11} elements. If each element requires to store a single precision value and a double precision matrix index, this size of matrix can be stored in $12 \times 10^{11} = 1.2 \times 10^{12}$ bytes ≈ 1.2 TB. It is expensive to use such a high memory volume in the computer and it is too slow to read as much data from hard disk in every iteration steps.

4.1 The Physical Background of the Model

The proton imaging based on the energy deposition of the protons passage through material, described by the theory of Bethe [27] and discussed with corrections in Ref. [28]. The Bethe or also called Bethe – Bloch equation describes the mean rate of energy loss by moderately relativistic charged heavy particles passage in material:

$$-\left\langle \frac{dE}{dx} \right\rangle = Kz^2 \frac{Z}{A} \frac{1}{\beta^2} \left[\frac{1}{2} \ln \frac{2m_ec^2\beta^2\gamma^2 T_{max}}{I^2} - \beta^2 - \frac{\delta(\beta\gamma)}{2} \right] \, , \tag{9}$$

where dE/dx is the mean energy transfer rate called also stopping power in the pCT literature, $K = 4\pi N_A r_e^2 m_e c^2$, Z and A is the atomic and mass number of the ion, respectively. The β is the velocity of the ion in the units of the speed of the light (v/c), m_e is the mass of the electron, c is the speed of the light, $\gamma = 1/\sqrt{1 - \beta^2}$, T_{max} is the possible maximal energy transfer between the ion and a free electron, I is the momentum of the ion and $\delta(\beta\gamma)$ is the density correction.

The path of the protons in the patient is described by multiply coulomb (MC) scattering [29]:

$$\theta_0 = \frac{13.6 \text{ MeV}}{\beta cp} q \sqrt{\frac{x}{X_0}} \left[1 + 0.038 \ln\left(\frac{x}{X_0}\right) \right] \, , \tag{10}$$

where θ_0 is the standard deviation of the Gaussian distribution of the scattering, p, βc and q are the momentum, velocity and charge (in units of elementary charge) of the particle and x/X_0 is the thickness of the material compared with its radiation length.

The tangential displacement of the protons as a result of the change in its direction by MC scattering during passage through material is investigated in Ref. [30],

$$\sigma_y = \frac{1}{\sqrt{3}} x \sigma_\theta \, , \tag{11}$$

where σ_y is the tangential displacement after passage a certain thickness of material represented by x. The direction of the particle changed with σ_θ standard deviation through the same path described by equation (10). The values of y and θ are correlated, with a coefficient of $\sqrt{3}/2$.

Nuclear interactions can happen during the passage as well, and they can have impact on the proton imaging as explained in details in Ref. [4], which is not described in this work.

The relative stopping power of the materials change with the energy of the proton, described by equation (9), so it can not be interpreted as a material property, which can be reconstructed by an imaging device. If one measure the stopping power of a material in units of stopping power in water with the same energy protons one can reach the relative stopping power (RSP) of the material. This is approximately independent of the energy of protons in the 50-250 MeV/u energy range relevant for pCT imaging. I have investigated this approximation for the relevant energy range and I found that the energy dependency of the RSP of the human body is less than 0.1 %. The result is presented on Figure 3.
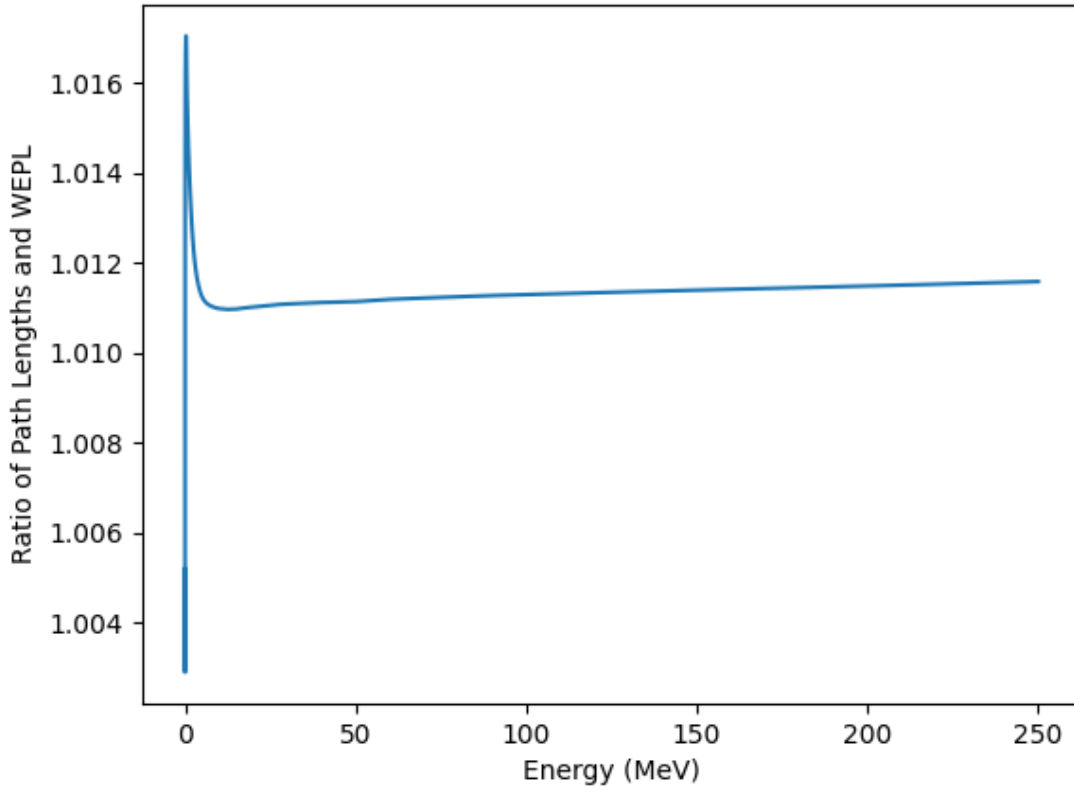
Figure 3: The constancy of the relative stopping power (RSP) of the main atoms of the human body in function of proton energy in relevant 50-250 MeV/u energy range. Note, energy is given here by setting atomic unit to 1.

4.2 Modeling of the Imaging

We use list-mode proton imaging, which means, that the detector measures: the energy loss, and the outcoming position and direction of each proton individually. For this data there are two important steps to reconstruct the image: the first is to investigate the trajectory of the protons in the patient, then, the second is to reconstruct the image from proton paths and energy losses.

The trajectory investigation based on the most likely path (MLP) of the protons, which

can be calculated based on the maximization of the probability of scattering of the protons during their path. A more computation efficient and not much less accurate solution is to approximate the MLP with a third-order spline, which was applied in this work as well [30]. The calculation of the elements of the system matrix (which are the interaction coefficients) is based on the probability distribution of the appearance of the real proton path around the estimated MLP of the protons. This method is new in the literature, but motivated by the published investigations about the MLP calculation techniques. I expect smoother and less noisy images from this method, but certainly the cost of the calculation per iteration is much higher, therefore result in slower convergence.

To investigate the performance of the image reconstruction algorithm I developed an imaging model, in which I can set the value of different type of uncertainties like the error of the measurement of the direction of protons or beam characteristics. This model investigated the path of the protons with third-order cubic splines as the imaging track, but I can set uncertainty on the beam position and for the measurement of the proton behind the patient. This practically means that the third-order spline will be fitted to slightly different incoming and outcoming information.

The energy deposition of the protons is modeled with the integration of the RSP of the phantom along the path of the protons. It integrates the RSP of voxels in around the MLP during the image reconstruction phase. On one hand, this solution makes it possible to test the image reconstruction with exactly the same approximations as data taking – if I set the uncertainties to zero. On the other hand, if I tend with the standard deviation around the MLP to zero, I can simulate the realistic situation, when the protons integrate through their MLP. By setting the realistic uncertainties, the model approximate a realistic data taking considering no nuclear interactions. The main properties of the real imaging, image reconstruction and modeling of imaging with and without uncertainties is listed in Table 1.

We note, the nozzle exit-izocenter and the detector-izocenter distance was set to be smaller than in the real experimental setup case to compensate the fact that the model takes into account spline between the nozzle exit and the detector. In a later version this can be improved,

and straight lines will be applied outside the phantom, and these distances can be set to realistic values.

	Real imaging	Imaging model 1 (as recon.)	Imaging model 2 (realistic)	Image reconstruction
Trajectory	MC scattering	Spline	Spline	Spline
Beam FWHM	7 mm	0 mm	7 mm	0 mm
Beam divergence	2.8 mrad	0 mrad	2.8 mrad	0 mrad
Dir. meas. err.	0.89 mrad	0 mrad	0.89 mrad	0 mrad
Multiply scattering	yes	yes	yes	yes
Scattering angle	22.0 mrad	22.0 mrad	22.0 mrad	22.0 mrad
Nuclear interactions	yes	no	no	no
$\sigma_{energy\ integration}$	-	1 mm	0.25 & 0.125 mm	1 mm
Nozzle exit - isocenter	500 mm [12]	150 mm	150 mm	150 mm
Detector - isocenter	250 mm [12]	150 mm	150 mm	150 mm
Resolution (n × n)	-	64	2048	64-512

Table 1: The main physical parameters were applied in the image modelling and reconstruction for simulating the interactions between protons and the material of the phantom.

4.3 The Numerical Model

In my model, I assumed that the interaction between protons and voxels is based on a Normal distribution around the MLP of the protons. I suspected that this consideration makes the linear problem less well-conditioned, but on the other hand I expected, that it will works better with relatively small number of protons typically measured in a pCT detector.

In order to speed up the calculations, fast parallel computing methods need to apply. Since linear algebra can be fast calculated in specific hardver. The graphical card, known as video cards including graphical processing unit (GPU) are widely used for such a methods. Recent program libraries are openly available for general purpose graphical processing units (GPGPU). I implemented my model in C++ and in CUDA, which latter is a GPU programming language based on C++ and developed by Nvidia [31]. The main focus of the code development is the

parallelization of the problem. There are two parallelization levels in the code and both are used during the image reconstruction.

1. The first level is the parallel computation of the protons, this solution is used for Hadamard ratio calculation. The current implementation runs on a single CPU core, which manage all the 14336 GPU threads on four Nvidia 1080Ti GPU card. This structure can be fast enough, since the machines' CPU only has to read the data from the storage and synchronize the GPU processes. If one CPU core would not be enough during the further optimization, the code can be parallelized more in CPU level based on the parallel processing of protons.

2. The second parallelization level is the parallelization of proton voxel interactions. This parallelization has the advantage of memory use when the Hadamard ration multiplied with the appropriate element of the system matrix has to be summarized by voxels.

Here, I apply and both parallelization methods for my recent work, which structural sketch of the developed algorithm is the following:

set M, L and T: number of trajectories, voxels and treads, respectively

set X to be unit vector, the vector of the voxel values

set dT and normT to L length zero vectors and Y is the vector of the measured data

repeat for N cycles, where N is the number of full iterations

    set $i = 0$, while $i < M/T$

(A) $H_t = Y_{i+t} / \sum\limits_{j}^{L} A_{i+t,j} \cdot X_j$, for all t, where t is the index of the thread, H is the Hadamard ratio and $A_{i+t,j}$ is the on the fly calculated interaction coefficient between the $i + t^{\text{th}}$ voxel and the jth proton trajectory

(B) set $j = 0$, while $j < T$

    $dX_k + = H_j \cdot A_{k,j}$ and $normX_k + = A_{k,j}$, for all k, where k is the index of voxels

$X_i = X_i \cdot dX_i/normX_i$ for all i, where i is the index of voxels

set dT and normT to zero vectors

save X vector as the resulted image

In the step (A) I applied the 1st parallelization, in the step (B) I used the 2nd parallelization. One can notice, that the elements of the system matrix are two times calculated in this structure. This is a necessary step, to preserve the computer memory storing the rows of the system matrix for each proton evaluated in an independent tread.

5 Results

In this section I will investigate the performance of the reconstruction algorithm, with the use of three different phantom. The first of them is the classical Shepp–Logan phantom [32], which I used to test the convergence of the algorithm in case of imaging with Model 1, which does not consider any uncertainties of the measurement. The second phantom is the Derenzo phantom [33], which I applied to investigate the resolution of the modeled imaging process with the Richardson–Lucy reconstruction algorithm. The third phantom is the CTP404 [34], which is used primarily to investigate the RSP accuracy of the imaging. Secondary this latter phantom was also for investigating the longitudinal position errors of the Bragg peak if I would irradiate a certain point of the CTP404 phantom and I would plan the dose based on the map taken by the modelled imaging system.

5.1 The Phantom Types

The first phantom I used is the Shepp–Logan phantom, which is presented in Figure 4(a). It is a commonly used, two dimensional phantom recommended by Larry Shepp and Benjamin F. Logan [32]. This model was used to test the convergence of the Richardson–Lucy deconvolution if I set the uncertainities of the imaging to zero. In this case I expect that the algorithm will tend to the exact solution.

The second phantom was used to test the spatial resolution of the imaging process is the Derenzo phantom in Figure 4(b) developed by Stephen E. Derenzo in Ref. [33]. This phantom has more variants, I used the so called cold rod variation, which is a water equivalent cylinder contains cylindrical holes filled with air spaced diameter distance from each other in a triangular structure. This phantom contains six regions with hole diameters of 1.5, 2, 3, 4, 5 and 6 mm.

The third phantom is called CTP404 presented in Figure 4(c), which is produced by The Phantom Laboratory [34]. The CTP404 phantom is designed to measure how accurately can an imaging system measures the properties of different materials, which is in my case the Relative Stopping Power (RSP). This phantom is an epoxy cylinder, which contains 8 inserts

with different materials and diameter of 12.2 mm. The RSP of the inserts and the epoxy was investigated by Alme et al. [11]. I evaluated the reconstructed average RSP in a 8 mm diameter circle in the middle of the inserts.
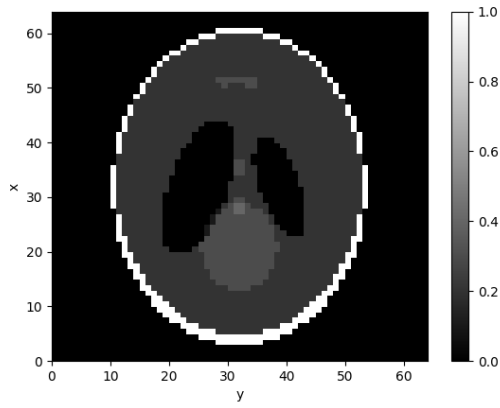
(a) Shepp–Logan phantom.
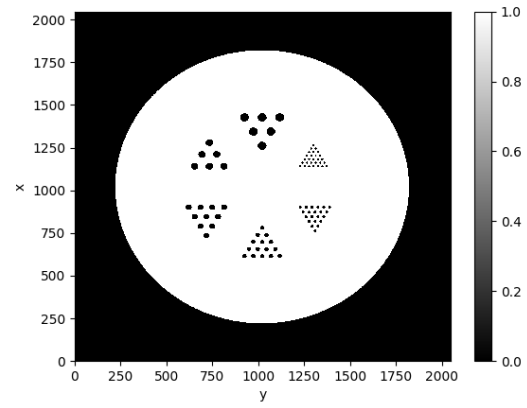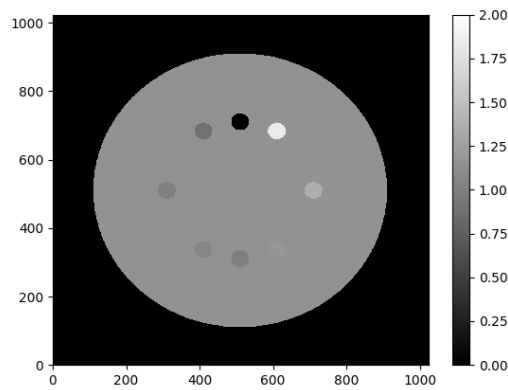
(b) Derenzo phantom.

(c) CTP404 phantom.

Figure 4: (a): Shepp–Logan phantom, (b): Derenzo phantom and (c): CTP404 phantom.

5.2 Test of convergence

First I tested the reconstruction algorithm with imaging Model 1, which is similar with the physical model of the image reconstruction. I used the 64×64 voxel Shepp-Logan phantom for this purpose and I measured the L2 or Euclidean norm of the difference between the reconstructed image and the phantom (with the same number of voxels in the phantom and image). I changed the standard deviation of the Normal distribution around the MLP between 1 mm and 10 mm.

In case of 1 mm the L2 norm tend zero, and reasonably gain up zero L2 norm within 1000 and 50000 iterations as it can be seen in Figure 5(b). The reconstructed images are presented in Figures 5(c) and 5(d), which are almost indistinguishable from the phantom in Figure 5(a). The difference becomes only visible as zoomed in the images, scaled into the RSP range of one region in the phatom in Figures 5(e) and 5(f).

The reconstructed images with 5 mm and 10 mm is presented in Figure 6. Theoretically L2 norm in case of 5 mm and 10 mm should also tend to zero, but based on the difference in the needed number of iterations between 1 mm and 2 mm it is not expected that they approaching zero L2 norm within reasonable number of iterations.

The first conclusion of this subsection is that the image reconstruction works well, and the problem is well-conditioned – at least in the case of $\sigma = 1$ mm. The second conclusion is that the number of needed iterations for the same convergence is quickly increasing with the value of σ parameter, which is most likely the sign of the deterioration of the conditioning of the linear equation system. The main question is if the conditioning of the problem depends in the σ set in the image reconstruction, which can be easily optimized, or depends on the uncertainties of the most likely path (MLP) determination, which is more difficult to improve.
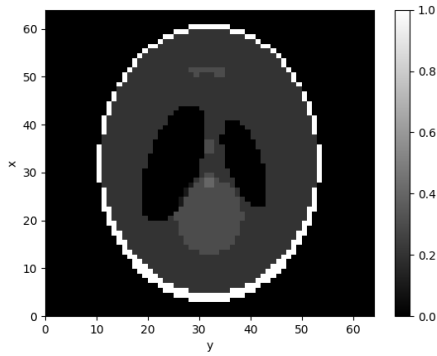
(a) Shepp–Logan Phantom
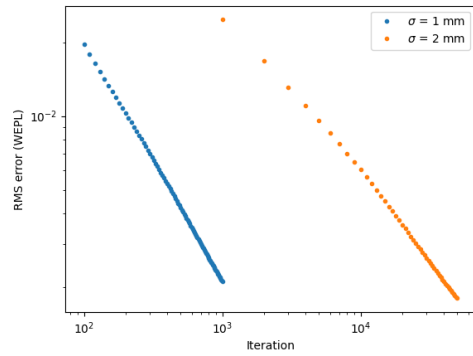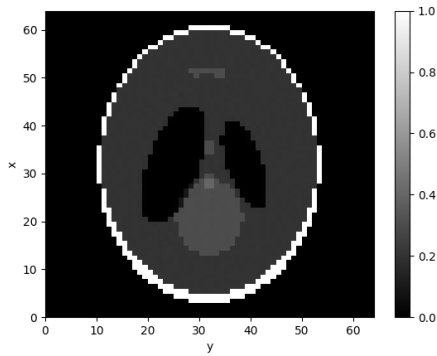
(b) Convergence

(c) $\sigma = 1$mm
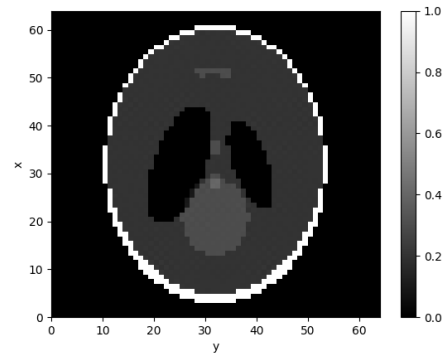
(d) $\sigma = 2$mm
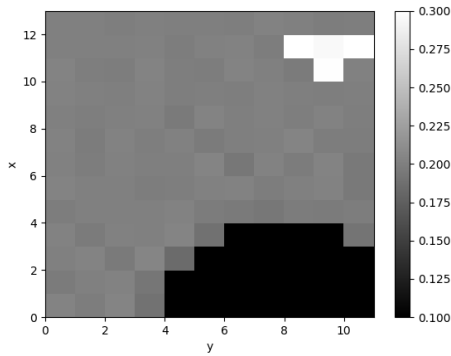
(e) Zoomed in, $\sigma = 1$mm
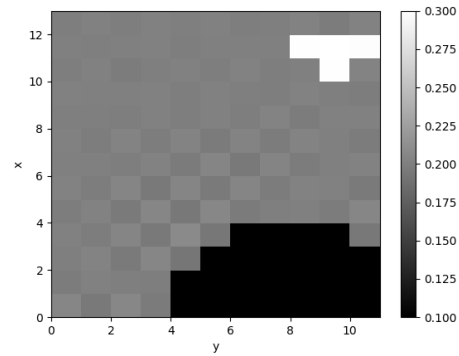
(f) Zoomed in, $\sigma = 2$mm

Figure 5: (a): Shepp - Logan Phantom, (b): convergence of the iteration, (c) and (d): reconstructed image with $\sigma = 1$ mm and $\sigma = 2$ mm, after 1000 and 50000 iteration, respectively, (e) and (f): zoom into a part of the image and into 0.1-0.3 RSP range of image in (c) and (d), respectively.
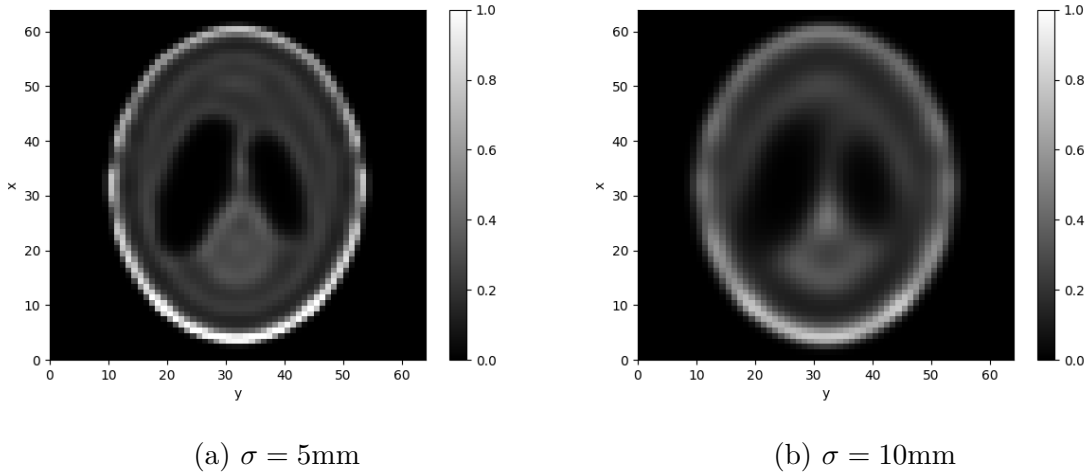
(a) $\sigma = 5$mm

(b) $\sigma = 10$mm

Figure 6: Reconstruction of 64×64 Shepp-Logan Phantom, after 1000 iteration, (a): $\sigma = 5$ mm and (b): $\sigma = 10$ mm.

5.3 Quality and Resolution

The goal of this section was to analyse the spatial and the RSP resolution (called as RSP accuracy) of the reconstructed images. In this work I defined the spatial resolution of the image as the full with at half maximum (FWHM) of the Normal distribution which would give the same peak-valley ratio as the convolution with the Normal distribution would give. This normal distribution is called point spread function (PSF) as well.

I tested the spatial resolution by applying the Derenzo phantom, with 3.6×10^6 protons, 512×512 image size and 250 iterations. Other parameters according to imaging Model 2 and image reconstruction in Table 1. The reconstructed phantom is visible in Figure 7(a).

I evaluated the resolution based on the valley/peak ratio in Figure 7(b) after subtraction of the background. Note that this phantom is a cold rod Derenzo phantom, which means that the density of the phantom is higher than the density of the rods. The valley and peak values become negative after subtraction of the background, and the one farther from zero is the peak; the ratio of the valley and peak become positive again. The ratio of the FWHM can be interpolated based on the curve visible in Figure 8. I find the FWHM of the PSF to be 4.3 mm.
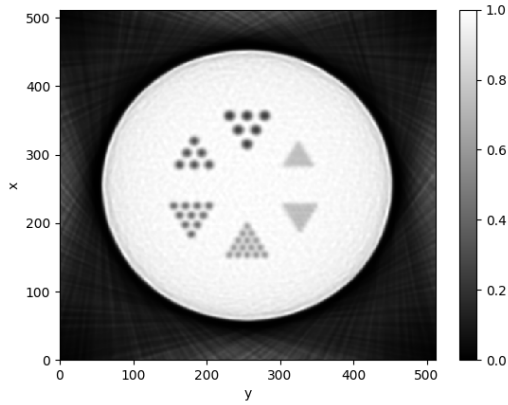
(a) Reconstructed Derenzo phantom.
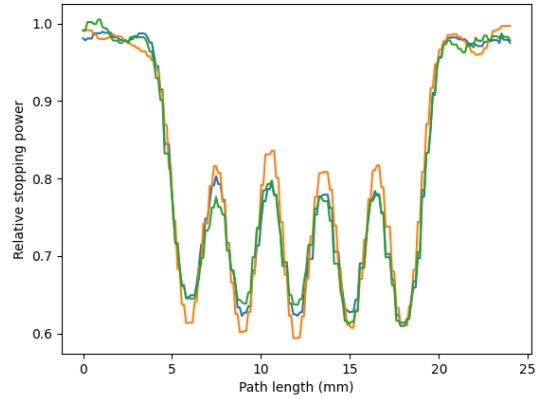
(b) RSP through lines.

Figure 7: (a): reconstructed Derenzo Phantom, (b): RSP value in lines goes through the rods with d = 3 mm. Number of voxels: 512, voxel edge size: 0.5 mm, all number of protons: 3.6×10^6, number of iterations: 250, and the rod diameters: 6, 5, 4, 3, 2, and 1.5 mm.
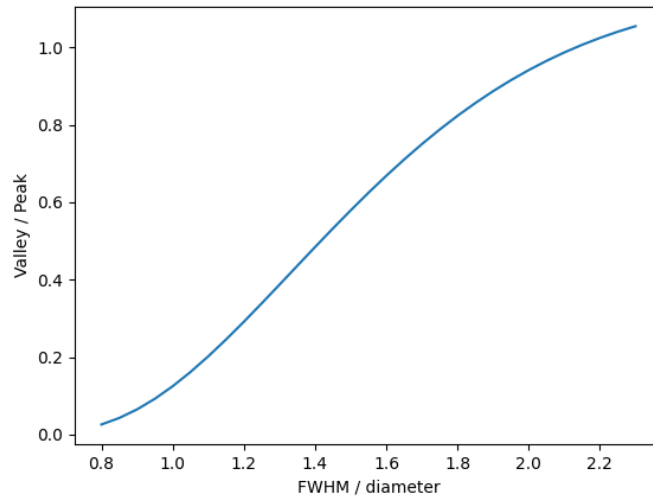
Figure 8: The valley-to-peak ratio in function of the ratio of the FWHM of the normal distribution and the diameter of the rods. This curve is calculated as the sum of two Normal distribution as the image of the rods, which would be exact for two Dirac delta and only an approximation of the case in the rods of the Derenzo phantom.

The RSP accuracy was tested with a phantom based on CTP404 phantom. I used the parameters in Imaging Model row of 2 in Table 1 for the imaging. The parameters of the image reconstructions was the following:

- Number of voxels: 512,

- Voxel edge size: 0.5 mm,

- Number of protons: 3.6×10^6,

- Number of iterations: 100, 200, and 300.

Remaining reconstruction parameters were set based on table 1. The list of the inserts and their ground true and reconstructed RSP value is visible in Table 2. I defined the reconstructed RSP value as the average RSP in the 8 mm diameter are in the middle of the inserts.

Material	Ground truth RSP	Reconstructed average RSP	Standard deviation of average RSP	Relative difference (%)
Air	0.0	0.1020	0.0270	-
Teflon	1.833	1.8033	0.0580	-1.62
Delrin	1.363	1.3379	0.0387	-1.84
Acrylic	1.179	1.1549	0.0336	-2.04
Water	1.0	0.9719	0.0289	-2.81
Polystyrene	1.0219	1.0312	0.0304	-2.49
LDPE	1.003	0.9851	0.0268	-1.78
PMP	0.886	0.8663	0.0378	-2.22
Epoxy	1.143	1.1300	0.0385	-1.14

Table 2: Inserts of the CTP404 like phantom. The ground true RSP value was set based on one of the previous work of the Bergen pCT Collaboration [11].
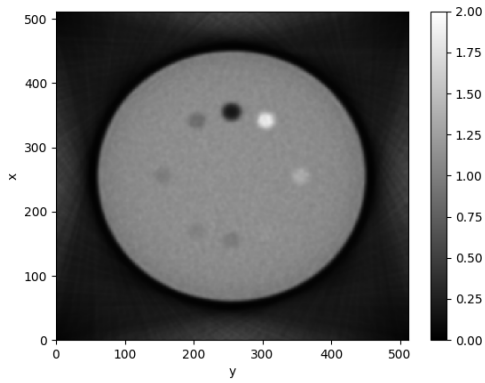
(a) CTP404 phantom – 100 iterations.
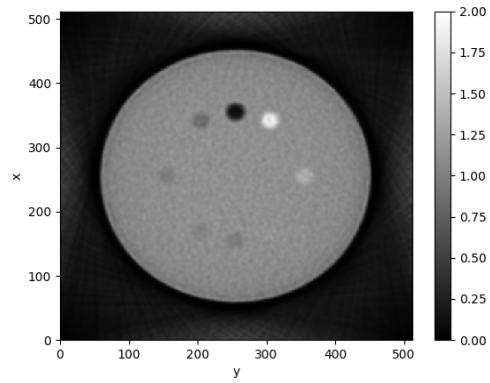
(b) CTP404 phantom – 200 iterations.
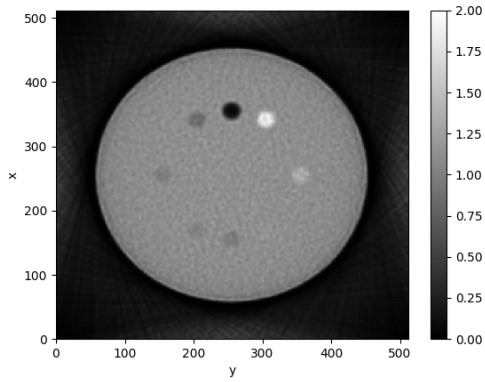
(c) CTP404 phantom – 300 iterations.
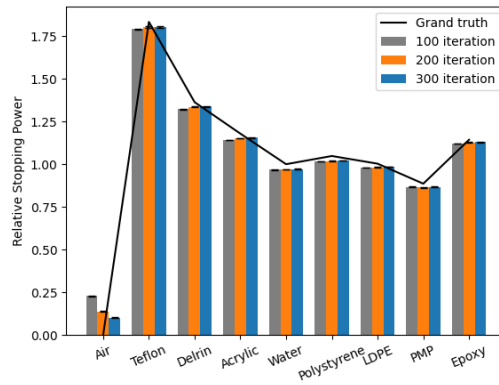
(d) Reconstructed and real RSP.
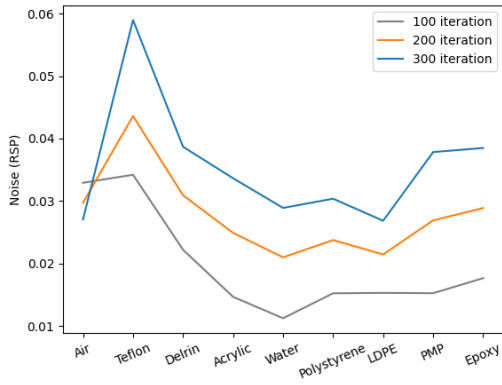
(e) RMS noise.
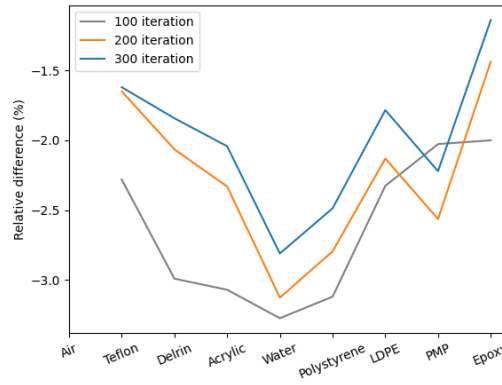
(f) Realtive error of RSP.

Figure 9: (a), (b) and (c): reconstructed CTP404 Phantom, (d): reconstructed and real RSP value, (e): RMS noise of the inserts and (f): relative difference of RSP values.

The accuracy of the RSP reconstruction of an object with a typical size of 12.2 mm is better than 3%, which is far from 0.4% published earlier by our group based on simulations with the same phantom [11]. The RSP accuracy is increasing with the number of iterations between 100 and 300 iteration asFigure 9(f) shows. At the same time the noise of the image is increasing as presented in Figure 9(e) which is also visible in the reconstructed images in Figures 9(a-c).

5.4 The Longitudinal Position Error of the Bragg Peak

Here, I introduce a clinically motivated investigation of image quality. The final purpose of the pCT images to represent an accurate RSP map about the patient for dose planning. Motivated by this purpose I tried to find a measure which characterizes the image quality from the point of view of clinical usefulness. I decided to compare the integrated RSP along a straight line to a certain point of the phantom from a certain direction.

The first step of this measure is to calculate the integrated RSP value along the straight line to the certain point, based on the reconstructed RSP map. This calculation of the energy for the proton beam, represented in water equivalent thickness (WET). The second step is to calculate the stopping point (which is almost the same with the maximum point of the Bragg peak) of the beam with the same energy in the same straight line, but based on the original RSP map of the phantom. The distance of this point and the certain point chosen in the beginning of the measure characterize the accuracy of the reconstructed RSP map. This measure can be automated and quickly evaluated for a numerous set of points in an arbitrary phantom.

This measure was investigated on the CTP404 phantom. First the central point of the phantom was chosen as a interest of the measure. The error of the Bragg peak is visible in Figure 10(a) in function of the angle measured from 12 hour position in Figure 4(c). The error is smaller than 3 mm and not correlated with the angle, so one can conclude that the reconstruction of the CTP404 is symmetrical. In Figure 10(b) a clear positive correlation is visible between the water equivalent path length (WEPL) of the protons and the error in the Bragg peak position, which can be described as the WEPL of the protons would be more or less the same without errors, so this behaviour is understood and does not contains information

about the image quality itself.

(a) Bragg Peak error - Angle (b) Bragg Peak error - WEPL
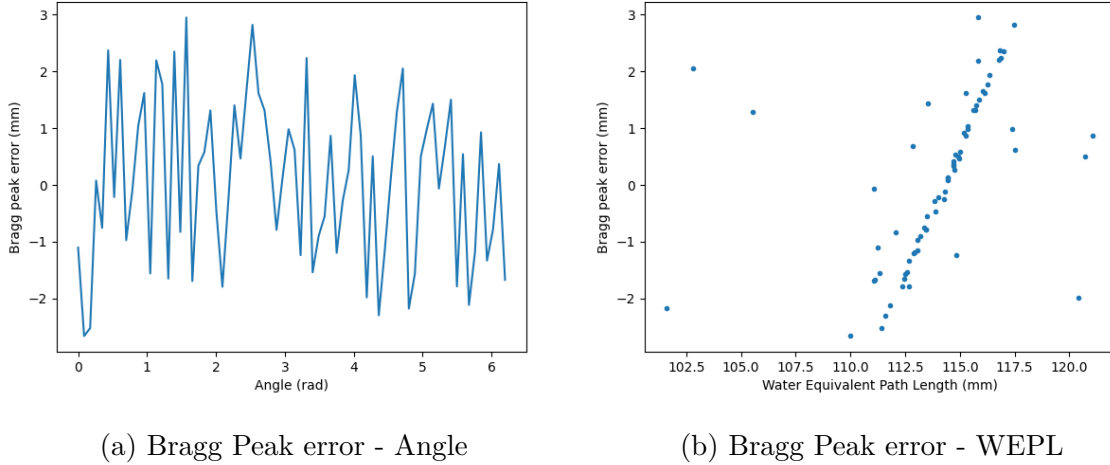
Figure 10: (a): the error of the Bragg Peak position in function of the beam direction and (b): the error of the Bragg Peak position in function of the path length of the proton before stopping. The beam aims the middle of the CTP404 phantom.

The second evaluated point was the middle of the water insert (6 hour position in Figure 4(c). The error of the Bragg peak is less than 4 % and visible in function of the angle in Figure 11(a). One can notice that there is some correlation between the angle and the error, which is confirmed by the Figure 11(b), where a clear negative correlation is visible between the WEPL of the protons and the error in the Bragg peak position. This correlation can not be simply describes with the nature of the errors, and it suggested that the RSP is overestimated in the middle of the phantom and underestimated in the edges of the phantom.
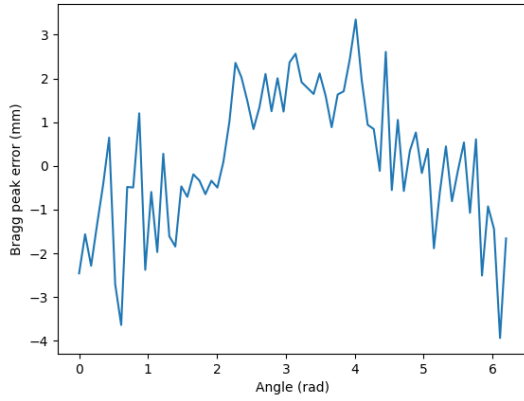
(a) Bragg Peak error - Angle
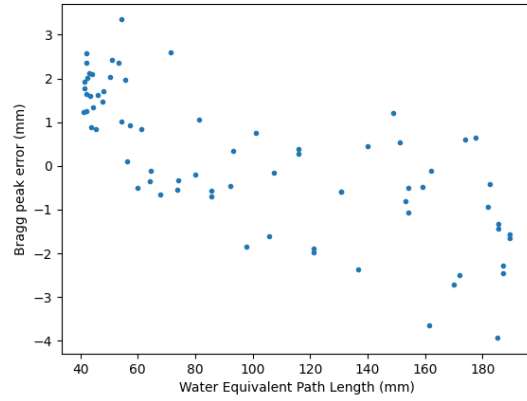
(b) Bragg Peak error - WEPL

Figure 11: (a): the error of the Bragg Peak position in function of the beam direction and (b): the error of the Bragg Peak position in function of the path length of the proton before stopping. The beam aims the middle of the water insert.

It has been showed that this type of measures can be useful for the evaluation of the image quality, so it worth the further investigation to develop, test and standardise this measure.

6 Summary

Thanks to the novel technologies in particle detection, accelerator techniques, and fast imaging and analysis algorithms, the role of the proton therapy has been more-and-more emphasized in the clinical practice during the recent years. The number of hadron therapy centers has been increased as well, indeed variety of the available hadron beams has been available. One of the key questions of this emerging field today is that how would be possible to reduce the safety margin around the tumor and reduce the dose of the healthy tissues? As I presented, the most promising direction for this aim is the use of proton CT technology during the dose planning. This can provide more accurate relative stopping power (RSP) map in the patient, than the standard radiology methods by applying X-ray. My recent TDK work is related to this research topic as member of the Bergen Proton CT international R&D collaboration.

My focus was on the pCT imaging and the investigation of the image reconstruction with pCT, as it has direct effect on the image quality. Nowadays, an improved version of the Diagonally Relaxed Orthogonal Projection method is used for image reconstruction in general. In my research I investigated the Richardson–Lucy algorithm for pCT image reconstruction for the first time, since it performs well in the field of emission tomography. To reach reasonable speed with this algorithm, a well structured, computational and memory efficient algorithm was implemented on four GPU cards provided by the Wigner GPU Laboratory.

My simulation results confirmed the applicability of the Richardson–Lucy algorithm. I tested this by using various phantoms: Shepp–Logan, Derenzo, and CTP404. The algorithm exactly restored the image if the imaging errors are turned off during the simulation. By turning on the errors in the process, the code gave reasonably good spatial resolution, and acceptable RSP resolution as well. I also found that the determination of the Bragg-peak position is quite precise even in this early stage of the development.

The presented results contributed to the image reconstruction developments of the proton CT for the Bergen pCT collaboration. Furthermore, the applied code development can be also apply in hadron therapy dose planning in general after further optimalization and speed improvements.

Acknowledgements

First of all I would like to thank Gergely Gábor Barnaföldi for believing in this work even in the most critical times. Without his advices and help I couldn't have walked the path that leads to these results. I would like to thank Mónika Varga-Kőfaragó for investing a huge amount of time and energy to launch my career. Last but not least I would like to thank Dávid Légrády for my knowledge about image reconstruction techniques.

References

[1] Hansen David, Seco Joao, Sangild Thomas, Ø Rensen S, Ø Rgen J, Baltzer Petersen Breede, E Wildberger Joachim, Verhaegen Frank and Landry Guillaume, A simulation study on proton computed tomography (CT) stopping power accuracy using dual energy CT scans as benchmark, Acta Oncologica, VOL. 54, 2015. DOI: 10.3109/0284186X.2015.1061212

[2] A. M. Cormack, Representation of a Function by Its Line Integrals, with Some Radiological Applications, Journal of Applied Physics VOL. 34, ISS. 9, 1963. DOI: 10.1063 _1.1729798

[3] A. M. Cormack, Representation of a Function by Its Line Integrals, with Some Radiological Applications. II, Journal of Applied Physics VOL. 34, ISS. 9, 1964. DOI: 10.1063_1.1729798

[4] Robert P Johnson, Review of medical radiography and tomography with proton beams, Reports on Progress in Physics, VOL. 81, NO. 1, DOI: 10.1088/1361-6633/aa8b1d

[5] Damjanovich Sándor, Fidy Judit and Szöllősi János, Sugárzások és kölcsönhatásuk az "élő" anyaggal (in Hungarian), Orvosi Biofizika, Medicina Könyvkiadó RT. 2007.

[6] J. F. Fowler, What can we expect from dose escalation using proton beams?, Clin Oncol (R Coll Radiol), DOI: 10.1053/clon.2002.0182

[7] Harald Paganetti, Range uncertainties in proton therapy and the role of Monte Carlo simulations, Phys. Med. Biol. VOL. 57, 2012, DOI: 10.1088/0031-9155/57/11/R99

[8] Helge Egil Seime Pettersen, Johan Alme, Gergely Gábor Barnaföldi, Rene Barthel, Anthony van den Brink, Mamdouh Chaar, Viljar Eikeland, Alba García-Santos, Georgi Genov, Silje Grimstad, Ola Grøttvik, Håvard Helstrup, Kristin Fanebust Hetland, Shruti Mehendale, Ilker Meric, Odd Harald Odland, Gábor Papp, Thomas Peitzmann, Pierluigi Piersimoni, Attiq Ur Rehman, Matthias Richter, Andreas Tefre Samnøy, Joao Seco, Hesam Shafiee, Eivind Vågslid Skjæveland, Jarle Rambo Sølie, Ganesh Tambave, Kjetil Ullaland, Monika Varga-Kofarago, Lennart Volz, Boris Wagner, Shiming Yang, Dieter Röhrich, Design opti-

mization of a pixel-based range telescope for proton computed tomography, Physica Medica, VOL. 63, 2019, DOI: 10.1016/j.ejmp.2019.05.026

[9] Christian Golnik, Fernando Hueso-González, Andreas Müller, Peter Dendooven, Wolfgang Enghardt, Fine Fiedler, Thomas Kormoll, Katja Roemer, Johannes Petzoldt, Andreas Wagner and Guntram Pausch, Range assessment in particle therapy based on prompt γ-ray timing measurements, Phys Med Biol, 2014, DOI: 10.1088/0031-9155/59/18/5399

[10] Christian Richter, Guntram Pausch, Steffen Barczyk, Marlen Priegnitz, Isabell Keitz, Julia Thiele, Julien Smeets, Francois Vander Stappen, Luca Bombelli, Carlo Fiorini, Lucian Hotoiu, Irene Perali, Damien Prieels, Wolfgang Enghardt, Michael Baumann, First clinical application of a prompt gamma based in vivo proton range verification system, Radiother Oncol, 2016, DOI: 10.1016/j.radonc.2016.01.004

[11] Alme, Johan and Barnaföldi, Gergely Gábor and Barthel, Rene and Borshchov, Vyacheslav and Bodova, Tea and van den Brink, Anthony and Brons, Stephan and Chaar, Mamdouh and Eikeland, Viljar and Feofilov, Grigory and Genov, Georgi and Grimstad, Silje and Grøttvik, Ola and Helstrup, Håvard and Herland, Alf and Hilde, Annar Eivindplass and Igolkin, Sergey and Keidel, Ralf and Kobdaj, Chinorat and van der Kolk, Naomi and Listratenko, Oleksandr and Malik, Qasim Waheed and Mehendale, Shruti and Meric, Ilker and Nesbø, Simon Voigt and Odland, Odd Harald and Papp, Gábor and Peitzmann, Thomas and Seime Pettersen, Helge Egil and Piersimoni, Pierluigi and Protsenko, Maksym and Rehman, Attiq Ur and Richter, Matthias and Röhrich, Dieter and Samnøy, Andreas Tefre and Seco, Joao and Setterdahl, Lena and Shafiee, Hesam and Skjolddal, Øistein Jelmert and Solheim, Emilie and Songmoolnak, Arnon and Sudár, Ákos and Sølie, Jarle Rambo and Tambave, Ganesh and Tymchuk, Ihor and Ullaland, Kjetil and Underdal, Håkon Andreas and Varga-Köfaragó, Monika and Volz, Lennart and Wagner, Boris and Widerøe, Fredrik Mekki and Xiao, RenZheng and Yang, Shiming and Yokoyama, Hiroki, A High-Granularity Digital Tracking Calorimeter Optimized for Proton CT, Frontiers in Physics, VOL. 8, 2020, DOI: 10.3389/fphy.2020.568243

[12] Jarle Rambo Sølie, Lennart Volz, Helge Egil Seime Pettersen, Pierluigi Piersimoni, Odd Harald Odland, Dieter Röhrich, Håvard Helstrup, Thomas Peitzmann, Kjetil Ullaland, Monika Varga-Kofarago, Shruti Mehendale, Ola Slettevoll Grøttvik, Viljar Nilsen Eikeland, Ilker Meric and Joao Seco, Image quality of list-mode proton imaging without front trackers, Phys. Med. Biol. VOL. 65, 2020. DOI: 10.1088/1361-6560/ab8ddb

[13] ALICE Collaboration, Technical Design Report for the Upgrade of the ALICE Inner Tracking System, Journal of Physics G Nuclear and Particle Physics. 41. 2014, available: https://cds.cern.ch/record/1625842

[14] H.E.S.Pettersen, J.Alme, A.Biegun, A.van den Brink, M.Chaar, D.Fehlker, I.Meric, O.H.Odland, T.Peitzmann, E.Rocco, K.Ullaland, H.Wang, S.Yang, C.Zhang, D.Röhrich, Proton tracking in a high-granularity Digital Tracking Calorimeter for proton CT purposes, Nuclear Instruments and Methods in Physics, VOL. 860, 2017, DOI: 10.1016/j.nima.2017.02.007.

[15] G. Tambave, J. Alme, G.G. Barnaföldi, R. Barthel, A. van den Brink, S. Brons, M. Chaar, V. Eikeland, G. Genov, O. Grøttvik, H.E.S. Pettersen, Z. Pastuovic, S. Huiberts, H. Helstrup, K.F. Hetland, S. Mehendale, I. Meric, Q.W. Malik, O.H. Odland, G. Papp, T. Peitzmann, P. Piersimoni, A. Ur Rehman, F. Reidt, M. Richter, D. Röhrich, A. Sudar, A.T. Samnøy, J. Seco, H. Shafiee, E.V. Skjæveland, J.R. Sølie, K. Ullaland, M. Varga-Kofarago, L. Volz, B. Wagner, S. Yang, Characterization of monolithic CMOS pixel sensor chip with ion beams for application in particle computed tomography, Nuclear Instruments and Methods in Physics Research Section A, VOL. 958, 2020, DOI: 10.1016/j.nima.2019.162626

[16] Ákos Sudár, Proton CT - új diagnosztikai eszköz a rákos daganatok kezeléséhez Fizika (in Hungarian), 34. OTDK, 2018, abstract available: https://otdk.hu/eredmenyek/62521

[17] Ákos Sudár, Investigating the temperature distribution of a hadron-tracking calorimeter, BME TDK, 2019, abstract available: http://tdk.bme.hu/GPK/EN4/j5

[18] Ákos Sudár, Measurement of the temperature distribution inside a calorimeter, BSc thesis, BME GPK Department of Energy Engineering, 2019, arXiv: https://arxiv.org/abs/2005.02830

[19] Johann Radon, Über die Bestimmung von Funktionen durch ihre Integralwerte längs gewisser Mannigfaltigkeiten, , Berichte über die Verhandlungen der Königlich-Sächsischen Akademie der Wissenschaften zu Leipzig, Mathematisch-Physische Klasse [Reports on the Proceedings of the Royal Saxonian Academy of Sciences at Leipzig, Mathematical and Physical Section], Leipzig: Teubner, 1917

[20] L. B. Lucy, An iterative technique for the rectification of observed distributions, The Astronomical Journal, VOL. 79, NO. 6, 1974. DOI: 10.1086/111605

[21] William Hardley Richardson, Bayesian-Based Iterative Method of Image Restoration, Journal of the Optical Society of America, VOL. 62, NO. 1, 1972. DOI: 10.1364/JOSA.62.000055

[22] Richard Gordon, Robert Bender and Gabor T. Herman, Algebraic Reconstruction Techniques (ART) for Three-dimensional Electron Microscopy and X-ray Photography, J. theor. Biol. VOL. 29, 1970. DOI: 10.1016/0022-5193(70)90109-8

[23] S. N. Penfold, R. W. Schulte, Y. Censor, A. B. Rosenfeld, Total variation superiorization schemes in proton computed tomography image reconstruction, American Association of Phisicists in Medicine, VOL. 37, ISS. 11, 2010. DOI: 10.1118/1.3504603

[24] Yair Censor, Tommy, Elfving, Gabor T. Herman and Touraj Nikazad, On Diagonally-Relaxed Ortogonal Projection Methods, SIAM J Sci Comput, 2008. DOI: 10.1137/050639399

[25] Gabor T. Herman, Fundamentals of Computerized Tomography, Second Edition, Springer, 2009. DOI: 10.1007/978-1-84628-723-7

[26] M. S. Kaczmarz, Angenäherte Auflösung von Systemen linearer Gleichungen (in German), Int. Bull. Pol. Acad. Sci. Lett. 35 355–7, 1937

[27] H.A. Bethe, Zur Theorie des Durchgangs schneller Korpuskularstrahlen durch Materie (in German), Annalen der Physik VOL. 397 ISS. 3, 1930, DOI: 10.1002/andp.19303970303

[28] C. Amsler et al. PL B667, Particle Data Group, 2008, available: https://pdg.lbl.gov/2008/download/rpp-2008-plB667.pdf (in 28.10.2021)

[29] C. Patrignani et al. Particle Data Group, Chin. Phys. C 40, 100001 2016, available: https://pdg.lbl.gov/2017/download/rpp2016-Chin.Phys.C.40.100001.pdf (in 28.10.2021)

[30] D. C. Williams, The most likely path of an energetic charged particle through a uniform medium, Phys. Med. Biol. VOL. 49, 2004. DOI: 10.1088/0031-9155/49/13/010

[31] Home page of NVIDIA CUDA: https://developer.nvidia.com/cuda-zone (in 27.10.2021)

[32] L. A. Shepp, B. F. Logan, The Fourier reconstruction of a head section, IEEE Transactions on Nuclear Science, VOL. 21, ISS. 3, 1974, DOI: 10.1109/TNS.1974.6499235

[33] S. E. Derenzo, T. F. Budinger, J. L. Cahoon, R. H. Huesman and H. G. Jackson, High Resolution Computed Tomography of Positron Emitters, IEEE Transactions on Nuclear Science, VOL. 24, NO. 1, 1977, DOI: 10.1109/TNS.1977.4328738

[34] Catphan® 600 phantom (containing CTP404 as a section), Phantom Laboratory, available: https://www.phantomlab.com/catphan-600 (in 27.10.2021)